Journal of Physics and Chemistry of Solids 157 (2021) 110206

Contents lists available at ScienceDirect

Journal of Physics and Chemistry of Solids

journal homepage: www.elsevier.com/locate/jpcs

Spin glass behavior and oxidative catalytic property of Zn_2MnO_4 from a metathesis driven metastable precursor

Shreya Kushwaha, Rajamani Nagarajan *

Materials Chemistry Group, Department of Chemistry, University of Delhi, Delhi, 110007, India

ARTICLE INFO

Keywords:
Oxides
Chemical synthesis
X-ray diffraction
Electron microscopy
Magnetic properties

ABSTRACT

The reaction of chloride salts of zinc and manganese with NaOH yielded a cubic spinel structured metastable precursor at room temperature, driven mainly by the salt elimination process's energetics. While classical drying processes failed to produce the monophasic oxide, recrystallization under the hydrothermal conditions yielded Zn_2MnO_4 in nano dimensions. The sample consisted of crystallites with an average 6 nm size and had a lattice dimension of 8.396 (13) Å. The selected area electron diffraction pattern reiterated the occurrence of cubic inverse spinel. The presence of fingerprint (A_{1g} and F_{2g}) modes of an inverse spinel at 663 and 561 cm^{-1} in the Raman spectrum further supported our finding. The TEM-EDS analysis confirmed the ratio of Zn: Mn as 1.95:1. The sample showed an optical bandgap of 2.54 eV. X-ray photoelectron spectral analysis established the existence of manganese in the IV oxidation state. The presence of Mn (IV) with small amounts of Mn (III) (up to 20%) was confirmed from the electron paramagnetic spectra recorded at room temperature and 77 K. An average oxidation state of 3.85 was deduced from the chemical redox titration experiments. The pseudocapacitive behavior of the sample was evident in cyclic voltammetric experiments. The sample exhibited paramagnetic behavior at 298 K within the applied magnetic field of ±50 kOe. In the temperature-dependent measurements, the zero-field and field cooled data points of Zn_2MnO_4 diverged at 13 K, suggesting a spin-glass behavior. An effective magnetic moment of 4.31 BM was deduced for the sample. The inverse spinel effectively catalyzed the oxidation of phenol. It facilitated nearly 100% degradation of bisphenol-A to salicylaldehyde and phenylethyl alcohol (as major products) in the presence of H_2O_2 and at a pH of 9.

1. Introduction

The scientific revolution brought by the nano-size regime, an intermediate between the finite molecule and the infinite condensed solid, is tremendous [1–9]. The quest of solid-state chemists to stabilize a metastable solid is endless, given the potential properties of these phases compared to the thermodynamical ones. Typically, nanomaterials are metastable structures, and chemists have adopted a bottom-up synthetic approach operating under near ambient conditions to fabricate them [1–9]. Majorly four types of reactions are employed to generate the nanostructures, viz., reduction, oxidation, hydrolysis, and precipitation. Additionally, the conventional heating process involving equilibrium conditions is replaced with unconventional energy sources such as microwave, ultrasound, and hydro/solvothermal to facilitate these metastable nanostructures' capture [1–9]. Albeit the unique advantages of other synthetic methods, hydrothermal synthesis is widely adopted for crystal formation and growth by chemical reactions and solubility changes above ambient temperature and pressure [10–15]. The recrystallization of metastable precursors, reshaped bulk materials, indirectly supplied reaction sources, and decomposition of a single-source precursor are the major synthetic strategies for fabricating inorganic nanostructures under hydrothermal conditions [10–15]. To generate multimetallic oxide nanostructures, metastable precursors, often produced rapidly in an aqueous solution via a co-precipitation reaction, can be subjected to recrystallization under high temperature-high pressure hydrothermal conditions.

We intended to apply the approach of generating a metastable precursor and further synthesize metastable cubic inverse spinel, Zn_2MnO_4, for the following reasons. The existence of five distinct phases, $ZnMn_2O_4$, $ZnMnO_3$, $Zn_2Mn_3O_8$, $ZnMn_3O_7$, Zn_2MnO_4 in the Zn–Mn–O ternary system, lower stability of the +4-oxidation state of manganese and its ability to undergo self-reduction into Mn (III) and Mn (II), and the energetic hindrance associated with the occupation of octahedral sites by zinc are the major issues surrounding the stabilization of inverse

* Corresponding author.
E-mail addresses: shreyakushwaha2010@gmail.com (S. Kushwaha), rnagarajan@chemistry.du.ac.in (R. Nagarajan).

https://doi.org/10.1016/j.jpcs.2021.110206
Received 22 February 2021; Received in revised form 18 May 2021; Accepted 29 May 2021
Available online 11 June 2021

cubic spinel Zn_2MnO_4 [16–19]. Hydrothermal reactions leading to oxide nanostructures are generally conducted in the presence of NaOH/KOH, which acts both as a base as well as a mineralizer to hasten up the reaction process. In the chosen system, Zn_2MnO_4, ZnO is the thermodynamically stable phase at NaOH's high concentration. Still, the basic conditions can immensely favor manganese oxidation (from II or III) to higher oxidation states. To overcome the stabilization of ZnO, one must use lower concentrations of NaOH and provide competing energetics. Salt elimination is one such energetics that can contend and pave the way for the generation of mixed metal hydroxide precursors and stabilize metastable nanostructures in the desired composition. The current work describes our efforts to realize inverse cubic spinel Zn_2MnO_4 in a nano-size regime and its extensive characterization using various physicochemical techniques. The catalytic role of Zn_2MnO_4 nanostructures in the oxidation of phenol and Bisphenol-A (BPA) further demonstrated manganese's existence in a higher oxidation state.

2. Experimental

2.1. Synthesis details

In the current set of reactions, 2 mmol of ZnO (Sigma Aldrich, 99%) was dissolved in 5–7 mL of HCl (Merck, 35%), to which 1 mmol aqueous solution of $MnCl_2{\cdot}4H_2O$ (Central Drug House, AnalaR ‹ 98%) was added under constant stirring. After homogenizing, a 1.2 M solution of NaOH (Fisher scientific, 97%) was added drop-wise till the pH attained a constant value of 12 as indicated by a pH meter (Eutech instruments pH 510). The resultant mixture was aged under continuous stirring for 12 h at room temperature. The precipitate was separated by centrifugation, washed with de-ionized water repeatedly till the washings did not show the positive test for chloride ions with the $AgNO_3$ solution. After this, 0.35 g of the precursor was transferred to a Teflon container (60 mL capacity), in which 45 mL of water was added. It was subjected to hydrothermal treatment at 150 °C for 24 h.

2.2. Characterization details

The powder X-ray diffraction (PXRD) patterns were collected over the two-theta range of 15–90° using a high-resolution X'Pert PANalytical diffractometer equipped with xenon detector employing Cu Kα radiation at a scan rate of 0.04°. The structural refinement of the PXRD pattern was performed using GSAS + EXPGUI software by the Rietveld method [20,21]. The sample's UV–visible spectrum was recorded by suspending the powder in ethanol using the Shimadzu-1601 spectrophotometer. The sample was mixed with KBr and pelletized to record the FTIR spectrum on PerkinElmer 2000 spectrometer. Raman spectrum was obtained using a Renishaw spectrometer employing a 514 nm laser (Ar^+). Electron microscopic analysis was carried out on ZEISS-Gemini SEM 500 (for FESEM) and the JEOL 2100 F microscope operating at 200 kV equipped with EDS attachment (for SAED and HR-TEM). X band electron resonance spectra were collected at room temperature and 77 K using JEOL JES-FA 200 ESR spectrometer. The chemical red-ox titration method was employed to estimate the average oxidation state (AOS) of manganese. Equimolar solutions (0.025 M) of $KMnO_4$ (Thomas Baker 95%) and oxalic acid (Central Drug House 99.5%) were prepared. Potassium permanganate was standardized using oxalic acid. The average oxidation state (AOS) of manganese was determined by oxalic acid-permanganate back titration [22,23]. We added 50 mg of the spinel to a mixture containing 5 mL of 1 M H_2SO_4 and 20 mL of standard oxalic acid solution. The solution was warmed to facilitate the reaction. It was back titrated with standardized potassium permanganate until the appearance of pale permanent pink color. Since all the manganese is reduced to its divalent form, the total manganese content is obtained by using the following equation

$$5C_2O_4^{2-} + 2MnO_4^- + 16H^+ \rightarrow 2Mn^{2+} + 10CO_2 + 8H_2O$$

The average oxidation state of manganese was obtained using the relation $5/2\ [C_2O_4^{2-}] = [Mn^{2+}]$.

Manganese (III) acetate dihydrate (Sigma Aldrich, 97%) and Mn (IV) solution (in-situ generated) were used as the standard samples to determine the amount of Mn (III) in the samples in addition to Mn (IV) spectrophotometrically [24]. The dissolution of both the samples was done in 6 M pyrophosphoric acid (Sigma Aldrich, 95%) and 12 M sulfuric acid (Merck, 98%) in a ratio of 2:1. Calibration curves were sketched using different Mn (III) concentrations and Mn (IV) solutions in pyrophosphoric acid. The absorbance values for both the samples were recorded at 398 and 510 nm. A similar procedure was followed for our sample. A CHI 600 D electrochemical setup equipped with a three-electrode system was used to measure the sample's cyclic voltammogram. The ITO sheet was coated with the sample, platinum wire, and Ag–AgCl electrodes as the working, counter, and reference electrodes, respectively. The measurement was done in a 1 M Na_2SO_4 neutral electrolyte solution. The potential window of 0–0.9 V (scan rate of 0.01 V/s) with a sensitivity factor of 0.1 was chosen. For coating the ITO substrate of 1 × 2.5 cm, the as-prepared spinel, acetylene black, and polytetrafluoroethylene (PTFE) were mixed (ratio of 8:1:1), followed by homogenization with an appropriate amount of *N*-methyl pyrrolidone (NMP) solution to make a slurry. The slurry-coated substrate was dried at 60 °C to evaporate the solvent. An automated surface area analyzer (Quanta chrome, Boynton Beach, FL) was used to estimate the samples' surface area by the BET method. The X-ray photoelectron spectroscopy measurements of the solid sample (XPS) were performed using PHI 5000 Versa probe II (FEI Inc.) with Ar^+ ion and C_{60} sputter gun at a pressure higher than 10^{-9} Torr. Magnetic measurements were conducted using a magnetic properties measurement system (MPMS XL Quantum Design USA).

2.3. Catalytic experiment details

The oxidation of phenol (Rankem, 99.5%) was attempted using Zn_2MnO_4 as a catalyst and H_2O_2 (Merck, 30% v/v) as an oxidizing agent. To 50 ml of 10^{-5} M of phenol, 1 ml of H_2O_2 solution, and 50 mg of catalyst were added. Aliquots were taken periodically, centrifuged, and the supernatant solution's absorbance was recorded on a UV–visible spectrometer (Shimadzu-1601). ^1H proton (400 MHz) and ^{13}C NMR (100 MHz) spectra of oxidized product from phenol were recorded on a Bruker advance-400 spectrometer using DMSO-d_6 as solvent TMS as an internal standard. The oxidative removal of the water pollutant, Bisphenol-A (Alfa Aesar, > 97%), was attempted in the presence of Zn_2MnO_4 and activated by H_2O_2. The pH of the reaction mixture was modified to 9 using NH_3 (1:1 v/v) solution. 50 ml of 4×10^{-5} M aqueous BPA solution was prepared, whose solubility was promoted by adding a minimum amount of absolute ethanol. To it, 1 ml of H_2O_2 and 50 mg of catalyst were added. The contents were thoroughly stirred, and aliquots were taken every 15 min. The mixtures were centrifuged, and the absorption spectra of supernatant solutions were recorded using a UV–visible spectrometer (Shimadzu-1601). The degraded products of BPA were analyzed by the GC-MS instrument (The accutoFGcV, JMS-T100GCV from JEOL) fragmentation pattern of the mass spectra using literature and library data of Agilent gas chromatography system (7890 A GC) having a capillary column (stationary phase: Polysiloxane; column length: 30 m; internal diameter: 0.25 mm; Film thickness: 0.25 μm) using helium as a carrier gas at a flow rate of 1 ml/min.

3. Results and discussion

Fig. 1(a) shows the PXRD pattern of the residue obtained after the addition of highly concentrated sodium hydroxide (source of polyatomic OH^- ions) to the aqueous solution of the chloride salts of zinc and manganese (monoatomic cations). NaCl's appearance in the PXRD pattern suggests that this reaction's driving force is salt elimination, as described by the following equation.

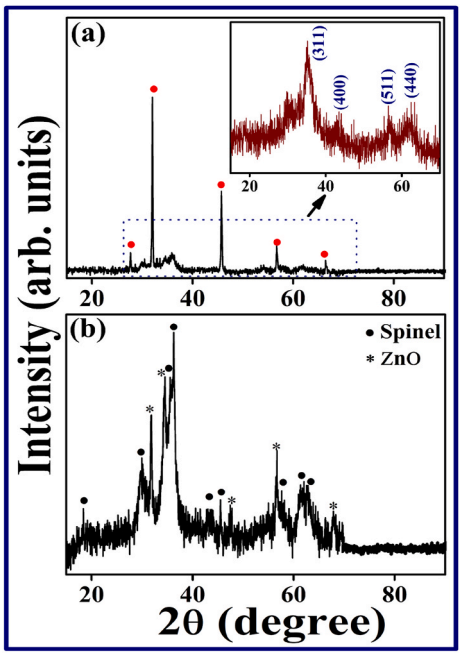

Fig. 1. (a) PXRD pattern of the precipitate obtained by the addition of NaOH to the aqueous solution of zinc and manganese chlorides (2:1 M ratio), and (b) PXRD pattern of the product after removing NaCl by washing with double distilled water followed by drying in a hot air oven at 70 °C for 12 h.

$$2\,ZnCl_2 + MnCl_2 \xrightarrow{NaOH} 2\,Zn(OH)_2 + Mn(OH)_x + NaCl.$$

The high concentration of alkali also facilitates faster nucleation of nano-sized crystals. The basic conditions can promote the oxidation of manganese (II). The metal hydroxides from the reaction may undergo further reaction through interdiffusion to result in mixed metal hydroxide. Interestingly, when aged over 12 h, the mixed metal hydroxide evolves structurally in a spinel-like arrangement, as revealed by its PXRD pattern after removing the NaCl (Inset of Fig. 1(a)). A similar observation is encountered when KOH is used as the precipitating agent (Fig. S1). When we try to perform the precursor's conventional drying in a hot-air oven at 70 °C, ZnO formation is noticed along with the mixed metal hydroxides (Fig. 1(b)). The reflections of ZnO and the spinel reflections persist even after calcining the precursor at 500, 600, 700, 800, and 850 °C in a flowing oxygen atmosphere for 3 h (Fig. S2). In earlier reports, the additional ZnO has removed by washing the samples with acetic acid [16]. We avoided washing with acetic acid as it might result in zinc-less compositions.

The precursor loses weight continuously with an increase in temperature up to 508 °C in its thermogravimetric trace (Fig. 2). We decided

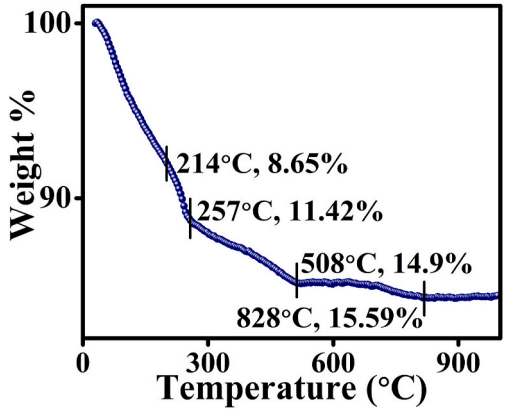

Fig. 2. Thermogravimetric trace of mixed metal hydroxide.

to overcome the extreme low stability (and high reactivity) of the mixed metal hydroxide precursor by transforming it (after repeatedly washing with double-distilled water) into a well-crystallized nanostructure by recrystallizing it under hydrothermal conditions (recrystallization of metastable precursors (RMP) route).

In this route, the crystals' growth in the nano-size regime occurs via the Ostwald ripening mechanism in which larger size crystals grow at the expense of smaller size crystals due to the crystals' high surface energy in the nano-size regime. It is evident from the increase in the average crystallite size (from 3 nm) to 6 nm after treating the precursor hydrothermally (Fig. 3(a)). The Le Bail refinement of the PXRD pattern in the $Fd\bar{3}m$ space group yields a cubic lattice dimension of 8.396 (13) Å, slightly higher than the values reported earlier (Fig. 3(a)) [16–18]. The higher lattice dimension of our sample may be due to higher amounts of Zn^{2+} ions in octahedra (0.74 Å) along with some amount of Mn^{3+} (high spin, 0.64 Å) in the spinel structural arrangement (Fig. 3(b)).

The vibration modes due to ZnO_4 tetrahedral units and Zn/MnO_6 octahedral units of the spinel structure manifest at 632 and 508 cm^{-1}, respectively, in the FTIR spectrum of the sample (Fig. 3(c)) [25]. Additionally, the vibrations of surface adsorbed carbonate species appear at 830 cm^{-1}. The Raman modes at 663 and 561 cm^{-1} signify the fingerprint (A_{1g} and F_{2g}) modes of an inverse spinel (Fig. 3(d) [26]. The aggregation of crystallites is noticed in the FESEM image (Fig. 4(a)). In the EDS spectrum, only zinc, manganese in the ratio of 1.95:1 is observed along with oxygen and rules out the inclusion of even trace amounts of sodium in the sample (Fig. 4(b)). Well-defined rings related to the *hkl* planes of the cubic spinel arrangement appear in the SAED pattern, confirming both the structure and crystalline nature of the sample (Fig. 4(c)). The lattice fringes with the distances of 2.53, 2.42, and 2.96 nm, observed in the HR-TEM image, correspond to (113), (322), and (022) *hkl* planes of a cubic spinel structural arrangement (Fig. 4(d)).

The positional parameter is calculated using the expression, $u = [(R_t + R_o)1/\sqrt{3}a + 0.25]$, where R_t = ionic radius of the tetrahedral site, R_o = ionic radius of oxygen ion, and a = lattice parameter. The estimated u for Zn_2MnO_4 (0.385) is closer to the ideal value expected for the ideal spinel (0.375). A small increment in the positional value may be due to tetrahedral site occupancy by larger Zn^{2+} ions [27].

The sample is subjected to X-ray photoelectron spectral analysis, and the results from these measurements are shown in Fig. 5. The exclusive presence of zinc, manganese and oxygen in the sample is inferred from

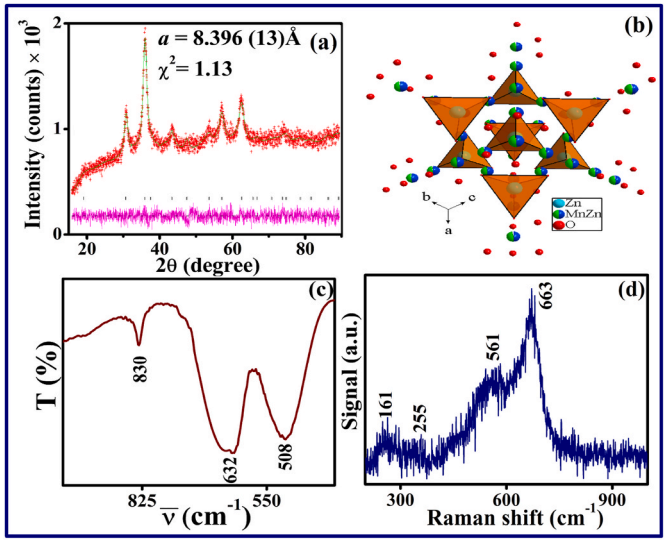

Fig. 3. (a) Le Bail refinement of the PXRD pattern, (b) Crystal structure of the spinel, (c) FTIR, and (d) Raman spectrum of the hydrothermally treated precursor after removing NaCl by washing with double distilled water.

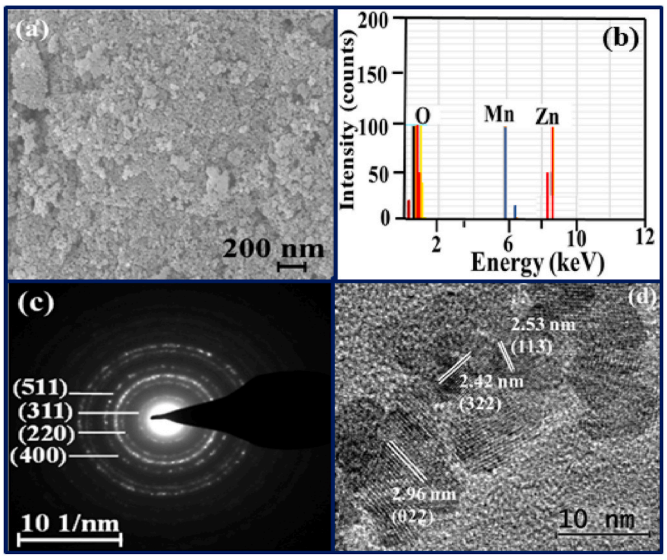

Fig. 4. (a) FESEM image, (b) EDS, (c) SAED pattern, and (d) HR-TEM image of Zn_2MnO_4.

the survey spectrum (Fig. 5(a)). There is no peak due to sodium in the survey spectrum, again reaffirming the absence of sodium in the lattice. The features appearing at 1018.8 and 1042.1 eV correspond to Zn $2p_{3/2}$ and Zn $2p_{1/2}$, respectively, and confirm Zn^{2+} in the sample (Fig. 5(b)) [28]. In the core-level spectrum of Mn *2p*, peaks at 640.0 and 651.7 eV emerging from Mn $2p_{3/2}$ and Mn $2p_{1/2}$ are seen (Fig. 5(c)) [29]. These features establish the existence of manganese in the IV oxidation state. The absence of any satellite peaks rules out the presence of even small amounts of Mn^{2+} in the sample [29]. The feature at 527.4 eV in O *1s* core-level spectrum corresponds to the lattice oxygen. The oxygen from the surface adsorbed hydroxides and carbonates appears at 528.8 eV (Fig. 5(d)) [28]. The feature at 282.3 eV in the C *1s* core-level spectrum is due to adventitious carbon used for charge correction reference, whereas the 286.2 eV feature belongs to the surface adsorbed carbonates [30]. The average oxidation state of manganese by the redox titration method (oxalic acid vs. potassium permanganate) comes out to be 3.85. We have also determined the Mn (III) concentration along with Mn (IV) spectrophotometrically. From the slope and intercept values of the calibration curves plotted between absorbance and concentration, the content of Mn^{3+} is estimated to be 20%, with the rest Mn (IV) in our sample. The UV–visible spectra and calibration curves of this quantitative estimation are given in Fig. S3 and S4, respectively.

The sample's UV–visible spectrum exhibits absorbance extending into the visible region (Fig. 6(a)). From the Tauc plot, an optical band gap of 2.54 eV is deduced (Fig. 6(b)). The optical bandgap of cubic inverse spinel Zn_2MnO_4 is reported here for the first time to the best of our knowledge. Fig. 6(c) shows the first derivative electron paramagnetic resonance plots of the spinel at both room temperature (RT) and 77 K. The spinel exhibits EPR signals at *g* values 2.057 and 2.138 at RT and 77 K, respectively. The signal at room temperature is broader as compared to the signal obtained at 77 K. The broadness may arise from the presence of a very minute amount of Mn^{3+} along with Mn^{4+} in the lattice, thereby modifying the Mn^{4+}-O-Mn^{4+} exchange kinetics to result in $Mn^{3+}{}_1$-O-$Mn^{4+}{}_2 \leftrightarrow Mn^{3+}{}_2$-O-$Mn^{4+}{}_1$ type of interactions at room temperature [31]. The interaction between Mn^{3+}-Mn^{4+} becomes prominent at room temperature due to the high thermal motion of electrons in both Mn^{3+} and Mn^{4+}, which results in the broadening of the EPR signal at RT than 77 K. The cyclic voltammogram of Zn_2MnO_4 in an aqueous solution is given in Fig. 6(d), in which a pseudocapacitive nature is evident from the response registered from the restricted negative and positive potential limits of 0–0.9 V. A similar observation is reported for the MnO_2 sample [32].

Various studies indicate the complex nature of magnetic properties of spinel oxides where contributions from the intrasite (A-O-A) and (B–O–B) and an intersite (A-O-B) superexchange interaction are seen. The distribution of non-magnetic and magnetic cations at the A- and B-sites determines the interaction's strength to a greater extent. The sample exhibits paramagnetic behavior at 298 K within the applied field range of ±50 kOe. Under similar fields, a hysteresis loop indicating weak ferromagnetic behavior of the sample is observed at 2 K (Fig. 7(a)). The coercivity and retentivity values of 1.7 kOe and 1.4 × 10^{-2} emu are deduced for the sample. The ZFC-FC plots in the temperature range of

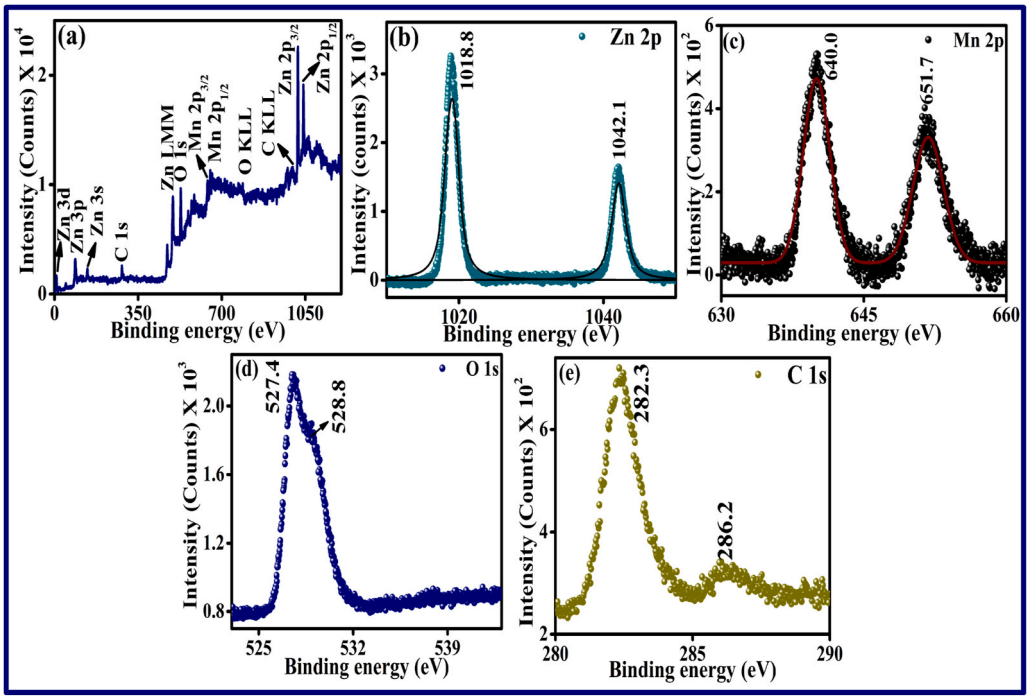

Fig. 5. (a) Survey XPS spectrum, and core-level spectra of Zn *2p* (b), Mn *2p* (c), O *1s* (d), C *1s* (e).

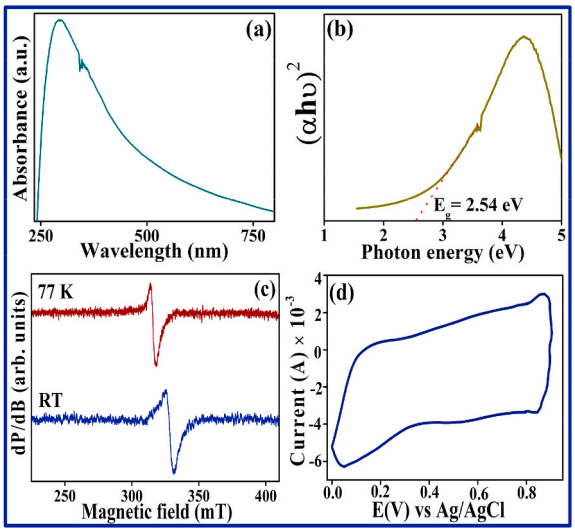

Fig. 6. (a) UV–visible spectrum obtained by suspended in ethanol, (b) Tauc plot for the estimation of the bandgap, X-band EPR spectrum recorded at room temperature (RT) and 77 K, and (d) cyclic voltammogram of Zn_2MnO_4.

2–340 K are presented in Fig. 7(b). Both plots overlap each other (an indication of paramagnetic behavior). They tend to show an increase in magnetization on decreasing the temperature until a bifurcation of ZFC and FC curves appear at 13 K. This divergence is due to the spin-glass behavior (inset of Fig. 7(b)) [18,33]. The position of non -magnetic cations determines the extent of magnetic exchange interactions. Thus, the hybridization of non-magnetic Zn^{2+} (3 d) and O 2p orbitals is essential in determining the material's ground state. Also, non-magnetic cations in octahedral sites disrupt the superexchange interaction mechanism among Mn^{4+}–O-Mn^{4+} in octahedra and results in spin glass frustrated systems [34]. Also, some Mn^{4+} at the surfaces may be reduced to Mn^{3+} by reacting with the atmosphere. The competing magnetic interactions between Mn^{4+} and Mn^{3+} are likely to contribute to the randomness [18]. The frustration index, calculated using the equation $f = \theta/T_c$, comes out to be 7 [35].

When the inverse of molar susceptibility is plotted against temperature, Curie-Weiss behavior is followed in the temperature range of 110–340 K (inset of Fig. 7(b)). The Curie-Weiss constant (θ_{CW}) value of −95.4 K indicates antiferromagnetic interactions between the Mn spins. The value of effective magnetic moment (in the linear region between 110 and 340 K), using the expression $C = \mu_{eff}^2/8$, is 4.31 BM. The slightly higher magnetic moment as compared to the spin-only value of Mn^{4+} (3.9 BM) is undoubtedly due to the presence of nearly 20% of Mn^{3+} in our samples. However, the amount of Mn^{3+} in our sample is far less than

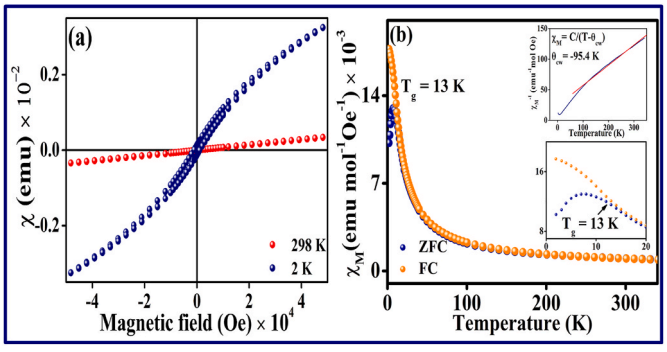

Fig. 7. (a) Plot of magnetization vs. the applied magnetic field, (b) magnetization vs. temperature of Zn_2MnO_4 at an applied field of 1000 Oe. Insets in (b) show the plot of χ^{-1} vs. temperature and the magnetization plot's expanded region.

the content reported by Blasco et al. in the case of $Mn_{1.3}Zn_{1.7}O_4$ (60%) and $Mn_{1.4}Zn_{1.6}O_4$ (80%) [18]. Their samples also had effective magnetic moments (4.85 and 5.10 BM), considerably higher than our value. Such a deviation is primarily due to the current synthetic approach of stabilizing Mn^{4+} under highly basic conditions and inhibiting the self-reduction to Mn^{3+} to an appreciable extent. In the nitrogen gas adsorption-desorption isotherms conducted on Zn_2MnO_4, a type-IV hysteresis is seen with a surface area value of 89 m^2/g (Fig. 8(a)). The mean pore-diameter value indicates the sample's mesoporous nature [36]. The catalytic role of Zn_2MnO_4 towards the oxidation of phenol is examined. The absorbance at 270 nm (n → π* transition) of phenol gradually disappears on the addition of the catalyst and H_2O_2 to phenol solution, and this is accompanied by the appearance of a new peak at 246 nm corresponding to benzoquinone (n → π* transition) (Fig. 8(b)). This entire transformation gets completed in 15 min ^1H and ^{13}C NMR show the formation of phenol to hydroquinone and benzoquinone (Fig. S5). The peak position values of ^1H NMR (δ 150.12, 116.11) and ^{13}C NMR (δ 8.69 and 6.56) correspond to hydroquinone, while the peaks with chemical shift values of ^1H NMR (δ 6.87) and ^{13}C NMR (δ 188.21 and 137.23) correspond to benzoquinone. The formation of hydroquinone and benzoquinone may be from the controlled and uncontrolled oxidation of phenol. The phenol oxidation mechanism may involve the radical generation from the reaction between Mn^{4+} of the spinel and the hydrogen peroxide, leading to its reduction to Mn^{2+} (probably present as manganous hydroxide). The acidic medium, provided by the natural acidity of hydrogen peroxide, may reduce Mn^{4+} to Mn^{2+}, which might be responsible for the oxidation of phenol to hydroquinone and benzoquinone [37].

The disintegration of BPA is attempted using Zn_2MnO_4 as a catalyst under Fenton-like conditions in a basic medium [38]. The hydroxyl ($OH^{\cdot}$) radicals are the reactive species involved when H_2O_2 is employed as the oxidant. The results of BPA disintegration carried out under basic pH conditions in the presence of Zn_2MnO_4 as the catalyst are presented in Fig. 8(c–e). The complete degradation of BPA is noticed under basic conditions (Fig. 8(c)). The control experiment proved that BPA did not undergo degradation in the absence of Zn_2MnO_4 (Fig. 8(d)). The reaction follows pseudo-first-order kinetics with a rate constant of 2.13 × 10^{-2} min^{-1} (Fig. 8(e)). The following arguments can be put forth to explain the catalytic function of Zn_2MnO_4. Under aerobic conditions, Mn^{4+} can be reduced to Mn^{2+} by the formation of Mn^{3+} as an intermediate. This redox shuttling may be responsible for making Mn^{4+} a powerful catalyst in the Fenton-like processes [38]. The first and second pKa values of BPA are 9.6 and 10.2. At lower pH values, BPA remains undissociated, but as the pH value increases to 9, its undissociated form becomes dominant and triggers the catalysis process [39].

The by-products of the catalytic degradation of bisphenol-A are examined by GC-MS analysis. The peaks 1 and 2 in Fig. 9(a) correspond to salicylaldehyde and phenylethyl alcohol, and they are the major products, 49 and 42%, respectively. The minor products are marked as 3, 4, and 5 and correspond to 2-phenyl ethyl acetate (5.2%), phenylethyl benzoate (1.8%), and phenylethyl phenylacetate (2%), respectively (Fig. (9(a)). The mass spectra of salicylaldehyde (base peak *m/z* value of 122), phenylethyl alcohol (base peak *m/z* value of 91), 2-phenyl ethyl acetate, phenylethyl benzoate, and phenylethyl phenylacetate (base peak *m/z* values of 104), are given in Fig. 9(b)–(f). The formation of various by-products arising from the multitude of reactions during the degradation of complex bisphenol-A is well known. The mechanism of this reaction can be described in the following steps. Hydrogen peroxide decomposes in the presence of catalyst into OH radicals, as shown in equation (1) [39], which react with contaminants. The OH radicals may further recombine to give oxygen and undergo oxidation/degradation of the pollutant BPA given by equation (2) [40].

$$H_2O_2 \xrightarrow{Catalyst)} 2OH \quad (1)$$

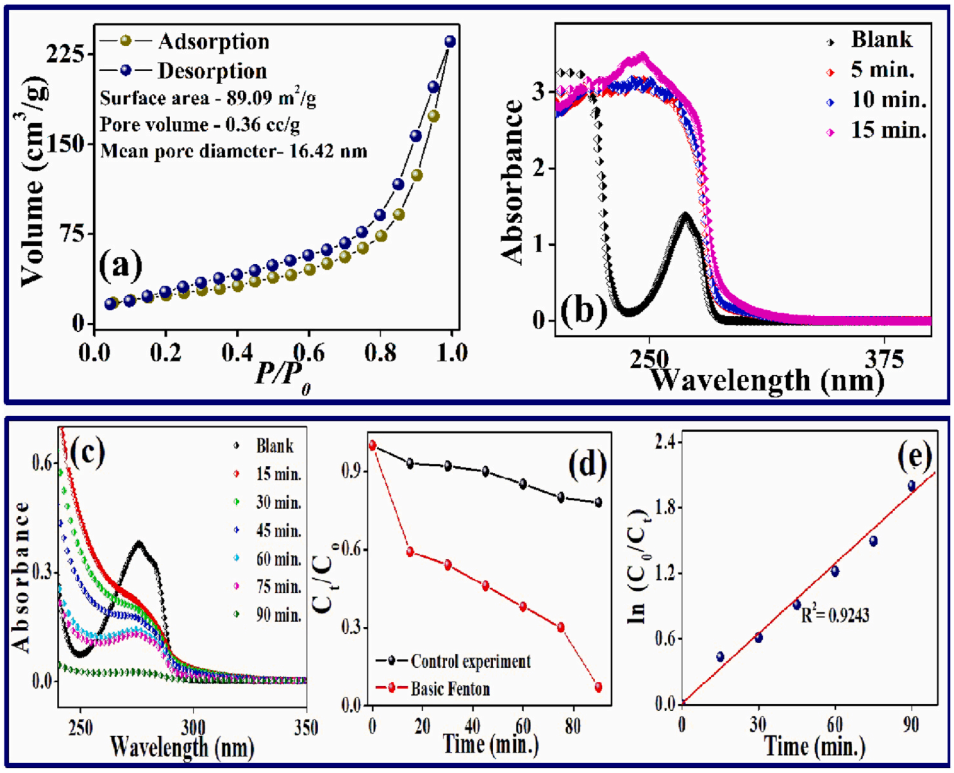

Fig. 8. (a) N_2 adsorption-desorption isotherms of spinel, (b), and (c) temporal changes in the absorbance spectrum of phenol and XO, respectively in the presence of spinel and H_2O_2, (d) plot of (C_t/C_0) vs. time and (e) plot of $\ln(C_0/C_t)$ vs. time for the degradation of BPA.

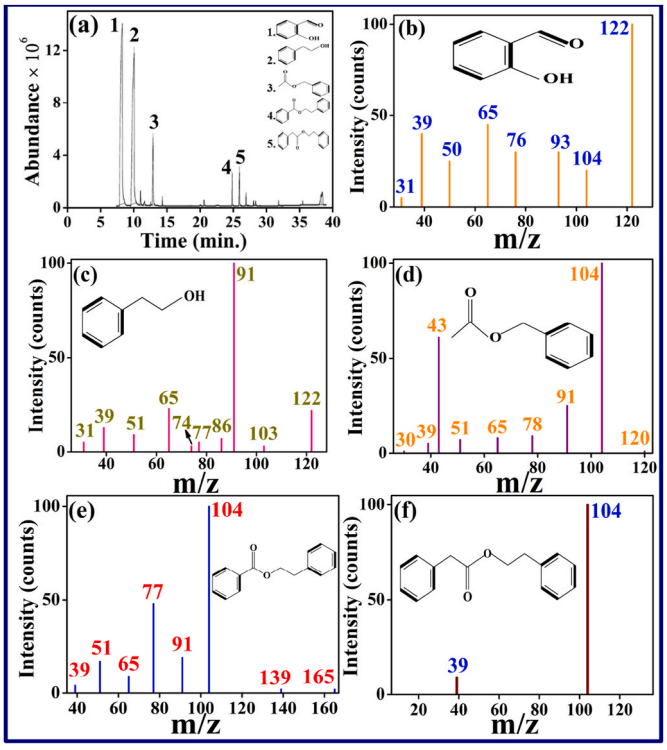

Fig. 9. (a) GC of the degradation products obtained after the Fenton-like reaction with bisphenol-A as a contaminant, and **(b)–(f)** mass spectra of compounds 1, 2, 3, 4, and 5 obtained after the degradation of bisphenol-A.

$$2OH\cdot + BPA \rightarrow \text{Degradation products} \ldots \tag{2}$$

In the presence of Mn^{4+} as the catalyst, the following steps may take place sequentially (equation 3-7) [39].

$$Mn^{4+} + H_2O_2 \rightarrow Mn^{2+} + \cdot OH_2 + H^+ \ldots \tag{3}$$

$$OH_2 \leftrightarrow H^+ + O_2^{-} \cdots \ldots \tag{4}$$

$$OH_2 + H_2O_2 \rightarrow \cdot OH + H_2O + O_2 \ldots \tag{5}$$

$$O_2^{-} + H_2O_2 \rightarrow \cdot OH + OH^- + O_2 \ldots \tag{6}$$

The ·OH may combine finally with the BPA molecule to form a multitude of products.

Thus, the overall reaction becomes

$$Zn_2MnO_4 + BPA \rightarrow \text{Degraded products} \ldots \tag{7}$$

4. Conclusions

The energetics of the metathesis reaction favored a metastable mixed-metal hydroxide, from which a zinc-rich inverse cubic spinel containing Mn (IV) in a nano-size regime was recrystallized under hydrothermal conditions. The process has overwhelming advantages such as high yield, simplicity of execution, greater control, uniformity of products, lower air pollution, and lower energy consumption. The existence of manganese in the IV oxidation state was established from XPS, EPR, and cyclic voltammetry measurements. The sample showed an optical band gap of 2.54 eV. It exhibited a pseudocapacitive behavior, quite similar to the electrochemical behavior noticed in MnO_2. The stabilization of the higher oxidation state of transition metals without the requirement of high oxygen pressures adds further significance to

this work. The sample's spin-glass behavior with a glass transition temperature of 13 K matched well with the literature reports, reinforcing the inverse cubic spinel arrangement consisting of non-magnetic zinc and magnetic manganese sharing the octahedral crystallographic sites [18]. The sample oxidized phenol entirely in 15 min. The oxidative degradation of BPA (100%) is catalyzed by the inverse spinel, from which salicylaldehyde and phenylethyl alcohol are identified as major products.

Author contribution

Shreya executed the experiments, collected and analyzed the data critically and prepared a rough write-up. Nagarajan has conceived the idea, involved in the polishing of the manuscript and management of the project.

Declaration of competing interest

The authors declare that they have no known competing financial interests or personal relationships that could have appeared to influence the work reported in this paper.

Acknowledgments

Financial support from SERB (EMR/2016/006131) Govt of India and Institute of Eminence Grant (IoE/FRP/PCMS/2020/27) from University of Delhi is gratefully acknowledged. SK thanks CSIR, Govt of India, for the research fellowship. The help extended by TIFR (Mumbai) India for magnetic measurements is acknowledged.

Supplementary Information

PXRD pattern of product from the reaction of chloride salts of zinc and manganese (2:1) with potassium hydroxide, PXRD patterns of the mixed metal hydroxide precursor calcined under flowing oxygen atmosphere at various temperatures, UV–visible spectra of Mn(III), Mn (IV) salts, and Zn_2MnO_4 in a mixture of pyrophosphoric acid (6 M) and sulfuric acid (12 M) and their calibration curves, ^1H NMR and ^{13}C NMR spectra of the products obtained from the oxidation of phenol.

Appendix A. Supplementary data

Supplementary data to this article can be found online at https://doi.org/10.1016/j.jpcs.2021.110206.

References

[1] C.N.R. Rao, A. Muller, A.K. Cheetham, The Chemistry of Nanomaterials: Synthesis, Properties, and Applications, Wiley-VCH Verlag GmbH & Co. KGaA, 2004.
[2] F. Caruso, Nanoengineering of particle surfaces, Adv. Mater. 13 (2001) 11–22.
[3] B.L. Cushing, V.L. Kolesnichenko, C.J. O'Connor, Recent advances in the liquid-phase syntheses of inorganic nanoparticles, Chem. Rev. 104 (2004) 3893–3946.
[4] H. Goesmann, C. Feldmann, Nanoparticulate functional materials, Angew. Chem. 49 (2010) 1362–1395.
[5] G.Y. Guo, J.S. Hu, L.J. Wan, Nanostructured materials for electrochemical energy conversion and storage devices, Adv. Mater. 20 (2008) 2878–2887.
[6] S.E.A. Gratton, S.S. Williams, M.E. Napier, P.D. Pohlhaus, Z. Zhou, K.B. Wiles, B. W. Maynor, C. Shen, T. Olafsen, E.T. Samulski, J. M Desimone, The pursuit of a scalable nanofabrication platform for use in material and life science applications, Acc. Chem. Res. 41 (2008) 1685–1695.
[7] R. Shenhar, V.M. Rotello, Scaffolds and building blocks, Acc. Chem. Res. 36 (2003) 549–561.
[8] S. Kinge, M. Crego-Calama, D.N. Reinhoudt, Self-assembling nanoparticles at surfaces and interfaces, ChemPhysChem 9 (2008) 20–42.
[9] W. Lu, C.M. Lieber, Nanoelectronics from the bottom up, Nat. Mater. 6 (2007) 841–850.
[10] W. Shi, S. Song, H. Zhang, Hydrothermal synthetic strategies of inorganic semiconducting nanostructures, Chem. Soc. Rev. 42 (2013) 5417–5743.
[11] M. Rajamathi, R. Seshadri, Oxide and chalcogenide nanoparticles from hydrothermal/solvothermal reactions, Curr. Opin. Solid State Mater. Sci. 6 (2002) 337–345.
[12] K. Byrappa, T. Adschiri, Hydrothermal technology for nanotechnology, Prog. Cryst. Growth Char. Mater. 53 (2007) 117–166.
[13] W.T. Yao, S.H. Yu, Recent Advances in hydrothermal syntheses of low dimensional nano architectures, Int. J. Nanotechnol. 4 (2007) 129–162.
[14] S.H. Feng, R.R. Xu, Recent advances in hydrothermal syntheses of low dimensional nano architectures, Acc. Chem. Res. 34 (2001) 239–247.
[15] C.S. Cundy, P.A. Cox, The hydrothermal synthesis of zeolites: history and development from the earliest days to the present time, Chem. Rev. 103 (2003) 663–702.
[16] S. L. Samal Menaka, K.V. Ramanujachary, S.E. Lofland, A. K. Ganguli Govind, Stabilization of Mn (IV) in nanostructured zinc manganese oxide and their facile transformation from nanospheres to nanorods, J. Mater. Chem. 21 (2011) 8566–8573.
[17] S.G. Fritsch, C. Chanel, J. Sarrias, S. Bayonne, A. Rousset, X. Alcobe, M.L. M. Sarrion, Thermal stability and electrical properties of zinc manganites, Solid State Ionics 128 (2000) 233–242.
[18] J. Blasco, J. Garcia, Stable cubic spinels in the Zn–Mn–O system in air, J. Solid State Chem. 179 (2006) 2199–2205.
[19] M. Peiteado, A.C. Caballero, D. Makovec, Diffusion and reactivity of ZnO–MnO_x system, J. Solid State Chem. 180 (2007) 2459–2464.
[20] A.C. Larson, R.B. Von Dreele, General Structure Analysis System (GSAS); Los Alamos National Laboratory Report LAUR, Los Alamos National Laboratory, Los Alamos, NM, 2004.
[21] B.H. Toby, EXPGUI, a graphical user interface for GSAS, J. Appl. Crystallogr. 34 (2001) 210–213.
[22] [Y. Zhu, X. Liang, H. Zhao, H. Yin, M. Liu, F. Liu, X. Feng, Rapid determination of the Mn average oxidation state of Mn oxides with a novel two-step colorimetric method, Anal Methods 9 (2017) 103–109.
[23] N. Kijima, H. Yasuda, T. Sato, Y. Yoshimura, J. Solid State Chem. 159 (2001) 94–102.
[24] H. Zhou, S. Mitamura, The Spectrophotometric determination of Mn (III) in the presence of Mn (IV), Anal. Lett. 25 (1992) 911–918.
[25] N. Garg, M. Mishra, Govind, A.K. Ganguli, Electrochemical and magnetic properties of nanostructured $CoMn_2O_4$ and Co_2MnO_4, RSC Adv. 5 (2015) 84988–84998.
[26] S.S. Mali, C.C. Shim, C.H. Hing, Highly porous zinc stannate (Zn_2SnO_4) nanofibers scaffold photoelectrodes for efficient methyl ammonium halide perovskite solar cells, Sci. Rep. 22 (2015) 11424.
[27] M.L.P. Le, P. Strobel, C.V. Colin, T. Pagnier, F. Alloin, Spinel-type solid solutions involving Mn^{4+} and Ti^{4+}: crystal chemistry, magnetic and electrochemical properties, J. Phys. Chem. Solid. 72 (2011) 124–135.
[28] R.A. Gaashani, R. Radiman, A.R. Daud, N. Tabet, Y.A. Douri, XPS and optical studies of different morphologies of ZnO nanostructures prepared by microwave methods, Ceram. Int. 29 (2013) 2283–2292.
[29] M.C. Militello, S.W. Gaarenstroom, Manganese dioxide (MnO_2) by XPS, Surf. Sci. Spectra 8 (2001) 200–206.
[30] J.F. Moulder, Handbook of X-Ray Photoelectron Spectroscopy: A Reference Book of Standard Spectra for Identification and Interpretation of XPS Data, Perkin Elmer, 1979.
[31] R. Stoyanova, M. Gorova, E. Zhecheva, EPR of Mn^{4+} in Spinels $Li_{1+x}Mn_{2-x}O_4$ with $0 \leq x \leq 0.1$, J. Phys. Chem. Solid. 61 (2000) 609–614.
[32] M. Toupin, T. Brousse, D. Belanger, Charge storage mechanism of MnO_2 electrode used in aqueous electrochemical capacitor, Chem. Mater. 16 (2004) 3184–3190.
[33] A. Kumar, A. Sanger, A.K. Singh, A. Kumar, M. Kumar, R. Chandra, Experimental evidence of spin glass and exchange bias behavior in sputtered grown α-MnO_2 nanorods, J. Magn. Magn Mater. 433 (2017) 227–233.
[34] X. Zhang, L. Wen, Y. Xu, K. Sun, X. Hao, Magnetic interactions in $ZnMnO_3$: active role of Zn $3d^{10}$ orbitals, in comparison with $MgMnO_3$, Inorg. Chem. 22 (2020) 16205–16214.
[35] D.W. Bruce, D. O'Hare, R.I. Walton, Functional Oxides, John Wiley, and Sons Ltd, 2010.
[36] F.J. Sotomayor, K.A. Cychosz, M. Thommes, Characterization of micro/mesoporous materials by physisorption: concepts and case studies, Acc. Mater. Surf. Res. 3 (2018) 34–50.
[37] D.B. Broughton, R.L. Wentworth, Mechanism of decomposition of hydrogen peroxide solutions with manganese dioxide. II, J. Am. Chem. Soc. 69 (1947) 744–747.
[38] A.D. Bokare, W. Choi, Review of iron-free Fenton-like systems for activating H_2O_2 in advanced oxidation processes, J. Hazard Mater. 275 (2014) 121–135.
[39] K. Lin, W. Liu, J. Gan, Oxidative removal of bisphenol A by manganese dioxide: efficacy, products, and pathways, Environ. Sci. Technol. 43 (2009) 3860–3864.
[40] Y.F. Han, F. Chen, Z. Zhong, K. Ramesh, L. Chen, D. Jian, W.W. Ling, Complete oxidation of low concentration ethanol in aqueous ethanol in aqueous solution with H_2O_2 on nano-sized Mn_3O_4/SBA-15 catalyst, Chem. Eng. 134 (2007) 276–281.